BLOOD FLOW IN CHRONIC STROKE LESIONS: AN IMPROVED MODEL OF BRAIN-BEHAVIOR RELATIONSHIPS

A Dissertation
Presented to
The Academic Faculty

By

Clara Glassman

In Partial Fulfillment
of the Requirements for the Degree
Master of Science in the
George W. Woodruff School of Mechanical Engineering
Department of Nuclear & Radiological Engineering and Medical Physics

Georgia Institute of Technology

August 2021

BLOOD FLOW IN CHRONIC STROKE LESIONS: AN IMPROVED MODEL OF BRAIN-BEHAVIOR RELATIONSHIPS

Thesis committee:

Dr. Lisa Krishnamurthy
Department of Physics and Astronomy
Georgia State University

Dr. C-K Chris Wang
Department of NRE and Medical Physics
Georgia Institute of Technology

Dr. Keith McGregor
Department of Neurology
Emory University

Dr. Tianye Niu
Department of NRE and Medical Physics
Georgia Institute of Technology

Date approved: June 23rd, 2021

Let us choose for ourselves our path in life, and let us try to strew that path with flowers.

Emilie du Chatelet

For my grandmama, Joy. The most inspiring woman I know.

ACKNOWLEDGMENTS

TABLE OF CONTENTS

LIST OF TABLES

LIST OF ACRONYMS

ASL Arterial Spin Labelling

ATT arterial transit time

BVMT Brief Visuospatial Memory Test

CASL Continuous Arterial Spin Labelling

CBF Cerebral Blood Flow

CSF Cerebrospinal Fluid

CVNR Center for Visual and Neurocognitive Rehabilitation

GM Grey Matter

HVLT Hopkins Verbal Learning Test

MRI Magnetic Resonance Imaging

PASL Pulsed Arterial Spin Labelling

pCASL Pseudo-Continuous Arterial Spin Labelling

RF radiofrequency

SCCAN Sparse Canonical Correlation Analysis for Neuroimaging

SNR Signal to Noise Ratio

TE Echo Time

TIGR Tissue Integrity Gradation via T2w T1w Ratio

TR Repetition Time

VLSM Voxel-Based Lesion-Symptom Mapping

WM White Matter

WUSTL Washington University in St. Louis

SUMMARY

A stroke has structural, physiological and behavioral consequences that significantly impact one's quality of life. Previously, the term lesion after stroke denoted that impacted tissue was completely and irrevocably non-functional [1]. However, improving imaging techniques, such as the novel approach Tissue Integrity Gradation via T2w T1w Ratio (TIGR), developed by Dr. Lisa Krishnamurthy, has made it possible to characterize gradients in degree of post-stroke structural damage with surviving tissue, offering new targets for rehabilitation.

In this work, we examine data evaluating the relationship between tissue integrity and Cerebral Blood Flow (CBF) within the lesion to further explore the physiology of lesioned tissue and determine its capability to improve prediction models of behavior post-stroke. Tissue integrity is quantified using a TIGR score ranging from 0 to 1, representing the severity of the structural damage from healthy to most damaged, respectively. CBF is quantified using the difference signal resulting from pulsed arterial spin labeling (PASL) magnetic resonance imaging (MRI) and applying a biophysical model to convert to absolute physiological units. We hypothesize that areas of lesion with greater tissue damage will also show a lower CBF, likely due to compromised cellular function and metabolism. We show that the average CBF in lesioned tissue is significantly lower than that of healthy tissue. We also show a significant decrease in CBF as the structural damage increases. We then evaluate their combined impact on functional outcomes after stroke, and find it to be significantly more robust than using structural damage alone.

CHAPTER 1

INTRODUCTION AND BACKGROUND

1.1 Stroke Induced Aphasia

A stroke has structural, physiological and behavioral consequences that can affect many systems of the brain, including motor, visual, executive function, and memory. One system that is often affected in left hemisphere middle cerebral artery strokes is the language system, resulting in aphasia in 40% of stroke cases, and persists in 60% into the chronic states (> 6 months post-stroke) [2], [3]. Unfortunately, it can be challenging to predict through imaging, as in some cases there are "unexpected lesion-to-deficit correlations," while "some stroke patients do not exhibit aphasia despite having a left-hemisphere lesion that affects classical language areas" [4].

Previously, the term lesion after stroke denoted that impacted tissue was completely and irrevocably non-functional, however clinical data shows that this assumption may be underinformed [1]. The impetus for this work is to demonstrate that there exists a damage gradient within the lesion that can be numerically labelled and physiologically supported. In this work we show how this numerical gradients representing damage can be calculated and confirmed by comparison to a physiological parameter. We then show how the additional inclusion of this physiological parameter can beter explain and predict behavioral deficits.

1.2 Magnetic Resonance Imaging

The imaging tools developed in this paper are built upon understanding the principles of Magnetic Resonance Imaging (MRI). MRI "relies on a core set of principles that were discovered by Rabi, Bloch, Purcell, and other pioneers" based on simple electromagnetic

interactions between protons and a static magnetic field, B_0 [5]. About 60% of the human body is water and the brain has a water content closer to 73%, thus the ability to image humans "rests on the ability to manipulate, with a combination of magnetic fields, and then detect, the bulk precession of the [proton of abundance, or] hydrogen spins in water, fat and other organic molecules [6], [7].

Each ^{1}H proton itself acts as a spinning gyroscope, and possesses a magnetic dipole moment of vector $\vec{\mu}$ as it rotates [5]. Without an external magnetic field, "each proton possesses a magnetic moment and angular momentum... [but] the spin axes of the protons are oriented randomly... and tend to cancel each other out [5]. In the presence of a magnetic field, the axes will align either parallel or anti-parallel to the external field and we will be left with a net magnetization, $\vec{M}$ [5]. While most protons will rest in the lower energy parallel state, the others rest in an anti-parallel state with the difference referred to as the 'spin excess':

$$\text{spin excess} \simeq N\frac{\hbar\omega_0}{2kT} \tag{1.1}$$

where N is the total number of spins present, $\hbar = \frac{h}{2\pi}$ where h is Planck's constant, k is the Boltzmann constant, and T is the temperature. The number of ^{1}H in the human body is large due to the high water content, such that the net magnetization is large enough to detect during MR imaging. The value of ω_0 is governed by the Larmor equation, shown below [7].

$$\omega_0 = \gamma B_0 \tag{1.2}$$

The Larmor equation is used to calculate the precession angular frequency for the proton, ω_0, and is determined by the field strength B_0 and the gyromagnetic ratio, γ, a constant value for the hydrogen proton in water of about 42.6 MHz/Tesla [7]. While we cannot measure the net magnetization directly, we can use indirect methods. By perturbing the spin

system away from equilibrium, known as *spin excitation*, measuring the signal from the resulting response provides information about the tissue properties [5]. This perturbation is done using radiofrequency (RF) pulses. The resulting signal generated from the perturbed protons will depend on the static field and go as:

$$\text{signal} \propto \frac{\gamma^3 B_0^2 \rho_0}{T} \tag{1.3}$$

(where ρ_0 is proton density) demonstrating that signal strength is dependent on field strength [7]. While the Signal to Noise Ratio (SNR) will increase and scanning times will decrease with a higher field strength, unfortunately physiological effects such as overheating, headache and nausea will also increase along with chemical shift and susceptibility artifacts, currently limiting the highest field strength approved by the US Federal Drug Administration for clinical use to 7T [8].

One "goal of imaging is to correlate a series of signal measurements with the spatial locations of the various sources" [7]. In MRI, spatial information (for example in x) is encoded by adding a spatially varying magnetic field gradient (in x) to the Larmor equation, to create "spectral components that represent spatial information" [7].

$$\omega(x) = \gamma B(x) \tag{1.4}$$

Such spectral information is transformed into an image using a 2D or 3D Fourier transform [7]. This phenomenon can also be utilized to "slice select" by exciting only a certain bandwidth of the precession frequencies with a band-limited RF pulse, as well as to image through common pulse sequence techniques such as gradient echo, and spin echo. These techniques are controlled by how many RF pulses are utilized, in what order, and for how long. The two common variables that are manipulated to generate different types of imaging results depend on Repetition Time (TR) and Echo Time (TE), where TR is the amount of time "between successive excitation pulses" and TE is "the time interval between an

excitation pulse and data acquisition (defined as the collection of data from the center of k-space)" [5].

After perturbing the protons, the regrowth and relaxation of M_z and M_{xy} respectively is determined by the Bloch equations [7]:

$$\frac{d\vec{M}}{dt} = \gamma \vec{M} \times \vec{B}_{ext} + \frac{1}{T_1}(M_0 - M_z)\hat{z} - \frac{1}{T_2}\vec{M}_\perp \qquad (1.5)$$

Where $\vec{B}_{ext}$ is the total external magnetic field, including B_0 and any additional applied magnetic field gradients. The time constants T1 and T2 govern the recovery of longitudinal magnetization, and the decay of transverse magnetization, respectively [5]. T1 is defined as the time it takes for M_z to recover to 63% of the initial value M_0 [5]. Sequence parameters TR and TE are optimized to set the contrast and highlight the signal from specific tissue types based on tissue T1 and T2.

1.2.1   T1w Imaging

Different tissue types, such as the brain's Grey Matter (GM), White Matter (WM), and Cerebrospinal Fluid (CSF), have different T1 constants associated with them due to the differences in water content and cellular composition. The T1 of tissue also changes in response to cellular changes, including degeneration and damage such as stroke. It is clinically of interest to identify different brain areas and to localize areas of damage. One method to image stroke is T1w imaging. The basis of T1 weighted (T1w) imaging is the regrowth of the net magnetization in the z direction. Solving the Bloch equation shown in Equation 1.5 for the initial boundary condition $M_z(0) = 0$ provides the following steady state solution:

$$M_z(t) = M_0(1 - e^{-t/T_1}) \qquad (1.6)$$

Provided that t=TR, Figure 1.1 shows that a short T1 recovers more quickly resulting in
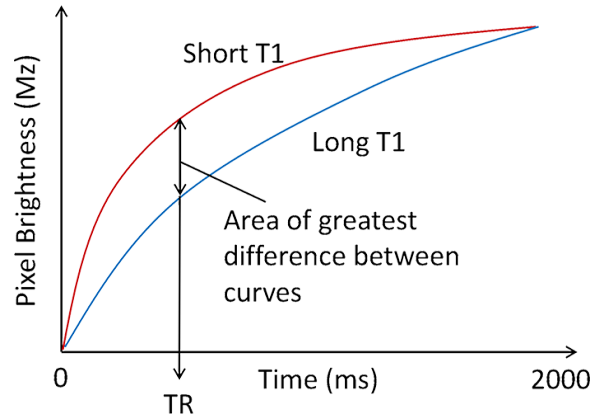
Figure 1.1: T1 regrowth. Image courtesy of radiologycafe [9]

a greater T1w signal, and a long T1 recovers more slowly, resulting in a smaller T1w signal. Because T1 is dependent on tissue type, tissues with a short T1 show up more brightly in the resulting T1w image.

T1 recovery is referred to as the spin-lattice interaction [7]. The spin-lattice interaction is the energy flow between spins and their external environment, where energy is in the form of heat [10]. T1w image contrast is optimized by taking advantage of the differences in T1 values between tissue types. Because CSF T1 is very long (4 sec), often a magnetization preparation pulse is played out prior to the image acquisition to suppress the CSF by choosing a TR and inversion time value corresponding to the zero crossing point [7]. Hence, in a T1w image, the CSF appears darkest, GM appears grey and WM appears brightest. An example of this can be seen in Figure 1.2a.

1.2.2 T2w Imaging

The brain's different tissue types also have different T2 values and can be differentiated on T2w imaging. Tissue changes due to damage can affect T2 differently than T1 because of differences in sensitivity to underlying cellular changes. T2w imaging is based on T2, which is dominated by spin-spin interactions between the protons, and quantified at the time that it takes for the transverse magnetization M_{xy} to decay to 37% of the initial value. A simple solution to the Bloch equation for the transverse magnetization (assuming TR
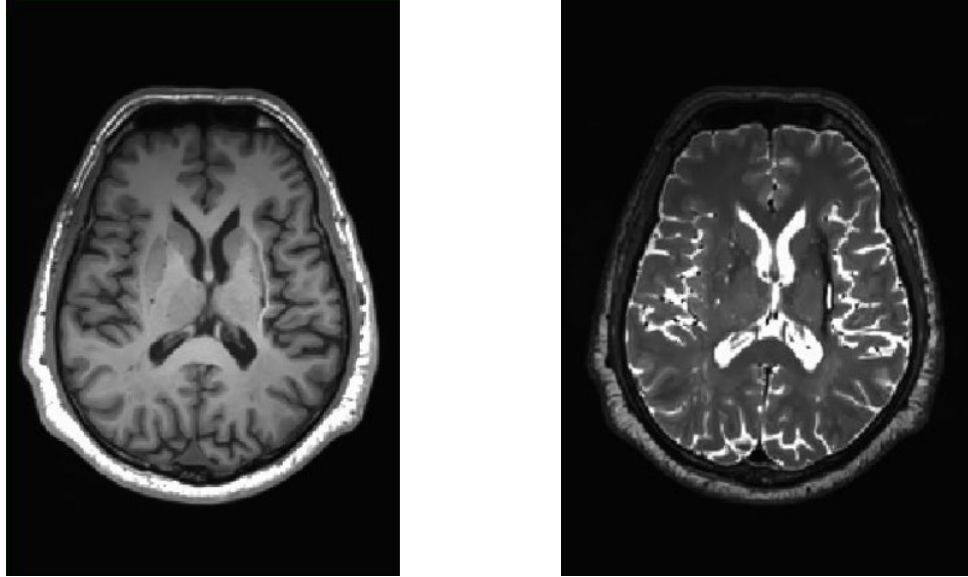
(a) T1w MRI of a stroke induced lesion.   (b) T2w MRI of a stroke induced lesion.

Figure 1.2: Example of T1w and T2w images on the same brain.

$>>$ T1) is [7]:

$$M_{xy}(TE) = M_0 e^{-TE/T_2} \tag{1.7}$$

T2w imaging requires a TE that isn't too long or too short to distinguish the signal between tissue types. This type of imaging is best achieved using a spin echo sequence [10].

CSF takes the longest to decay and will appear the brightest, GM will appear as an intermediate signal, and WM will be the darkest. A rough table of T1 and T2 values in a field strength of 3 Tesla are shown in Table 1.1. Because of the brightness of CSF, T2w imaging is useful in detecting pathology. An example of a T2w image is shown in Figure 1.2b.

1.2.3 TIGR

As seen in Figure 1.2a and Figure 1.2b, T1w and T2w images help detect pathology and are routinely used in the clinic. Recently, it was shown that there is hidden information within
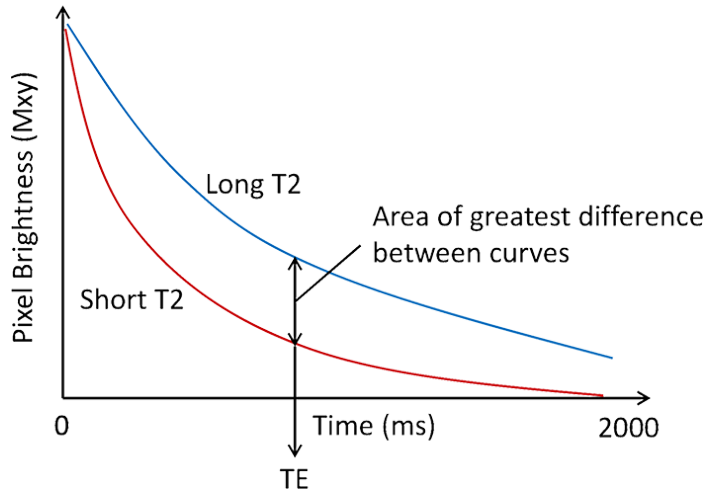
Figure 1.3: T2 decay. Image courtesy of radiologycafe [9]

Table 1.1: Table of measured T1 and T2 values for time constants in milliseconds at 3 T from Lu et al. [11]. FWM = Frontal White Matter, OWM = Occipital White Matter, FGM= Frontal Grey Matter, and OGM = Occipital Grey Matter.

Region	T1 (ms)	T2 (ms)
FWM	699 ± 38	69 ± 2
OWM	758 ± 49	81 ± 3
FGM	1209 ± 109	88 ± 3
OGM	1122 ± 117	79 ± 5

these routinely used scanning techniques. Previously, there was no "uniformly accepted, objective non-invasive methodology to identify pericavitational areas within the chronic stroke lesion... To fill this gap, [Dr. Krishnamurthy et al.] develop[ed] and validate[d] a novel Magnetic Resonance Imaging (MRI) methodology to objectively quantify the lesion core and surrounding pericavitational perimeter, which [they refer to as] TIGR" [12].

TIGR is able to "identify tissue composition changes within the stroke lesion, and... delineate lesion core from pericavitational areas," creating a damage gradient within and surrounding the lesioned area [12]. This is of utmost importance because understanding the pericavitational damage can allow the visualization of what tissue is still viable and can be targeted with functional therapy to stimulate growth of neural dendrites previously lost to stroke [13]. Perhaps most importantly, "T1w and T2w scans are routinely collected in the clinic", which means that TIGR maps can readily be incorporated in clinical settings

7

without additional imaging costs or patient burden" [12].

An example of a TIGR scoring map overlaid on a lesion can be seen in Figure 1.4b in contrast to the T1w view of the lesion in Figure 1.4a. While the T1w image provides a means of localizing the lesioned area, the TIGR score provides both a visualization of the damage gradient as well as an objective quantification of tissue damage spanning from zero to one, with zero being healthy tissue and one being most damaged.
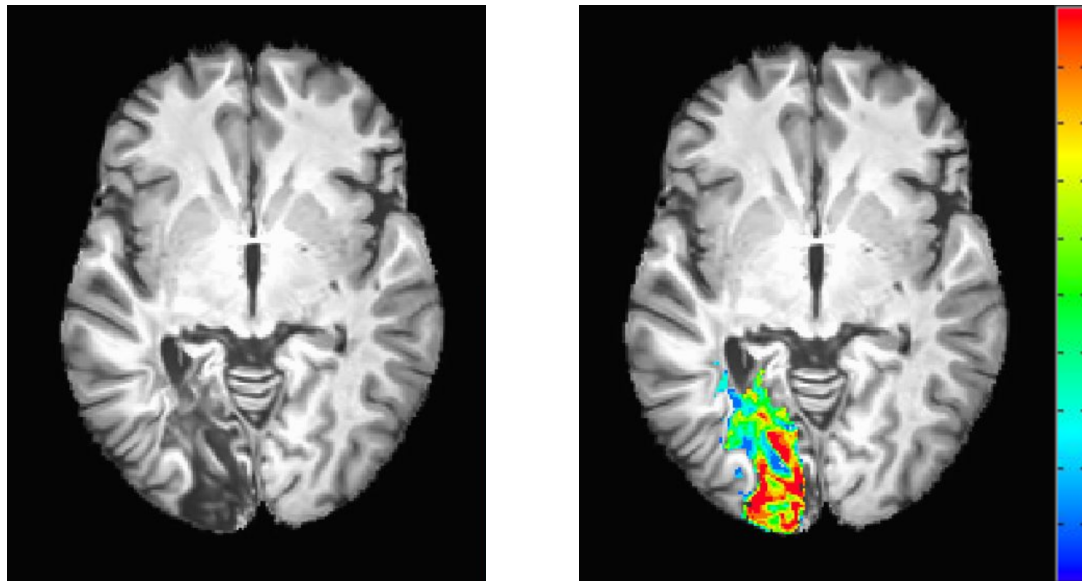
(a) MPRAGE in MNI space.   (b) TIGR scoring overlaid on MPRAGE

Figure 1.4: Example of a lesion in an MPRAGE image (in MNI space) versus the TIGR score overlaid on a an MPRAGE image. The TIGR score provides a numerical gradient to the damage as seen by the color bar that goes from 0.1 (blue=least damaged) to 1.0 (red=most damaged).

1.2.4   Arterial Spin Labeling MRI

While T1w and T2w images can depict anatomical damage within the brain, we hypothesize that structural damage alone does not provide enough information to fully describe or predict behavioral deficits. Hence, even with the novel imaging modality TIGR where we can quantify structural damage inside of a lesion, we need additional physiological parameters to fully describe tissue viability and its relationship to behavior. One physiological parameter that may aide in assessing tissue health is Cerebral Blood Flow (CBF), because

"tissue function depends heavily on perfusion, a process that brings nutritive blood supply to the tissue through the arterial system and drains the metabolic by-products into the veins" [14]. However, CBF can be very challenging to quantify, especially in a non-invasive, accurate manner without the usage of intravascular contrast agents [15].

Arterial Spin Labelling (ASL) MRI is a method to quantify blood perfusion throughout the brain and can then be converted into absolute physiological units using a biophysical model. ASL imaging can "provide non-invasive images of local CBF with better spatial and temporal resolution than any other technique, including nuclear medicine methods" and can be divided into three main types: PASL, pCASL, and CASL [15]. The ultimate goal of all three methods is to "measure CBF [or] the rate of delivery of arterial blood to a local brain voxel in an imaged slice of interest" in units of mL/100 g/min [15].

While specific types of ASL differ in the exact pulse order and method, the overall process for all types is similar. They all must start with a 180° RF pulse that inverts the magnetization of the water within the blood [15]. After some amount of time, referred to as the inversion time (TI) to allow the tagged blood to reach the tissue in the slice of interest, an image is taken [15]. The volumes of images collected when the incoming arterial blood is labelled are referred to as the tagged images, or "label" images. This process is repeated without the inversion of magnetization creating the "control" images. Then, computing the difference image (= control - label) provides an image that contains the "signal difference of arterial blood" and "the resulting ASL difference image signal is directly proportional to how much arterial blood was delivered" [15]. This perfusion image can then be utilized to calculate the CBF using a mathematical modelling specific to the ASL sequence utilized. The most basic model is a modified version of the Bloch Equation introduced in 1992 "combining kinetics and relaxation" by Detre et al. [16], [15].

$$\frac{dM(t)}{dt} = \frac{M_0 - M(t)}{T_1} + fM_A(t) - \frac{f}{\lambda}M(t) \qquad (1.8)$$

In this equation $M(t)$ is the longitudinal relaxation of the tissue "with an equilibrium

value of M_0", $M_A(t)$ is the "longitudinal magnetization of the inflowing arterial blood", f is the perfusion rate, and λ is the "partition coefficient of water molecules between tissue and blood" [14], [15]. While Buxton et. al 2009 points that this equation serves as a basis for the early ASL quantification experiments, it is based on the incorrect assumption that the magnetically "labeled water delivered to the brain immediately mixes with the large pool of tissue water" [15]. This assumption ignores the reality that there is a timeframe required for blood to travel from the labeling point to the point of perfusion, the arterial transit time (ATT). This is a non-negligible value that is a "primary source of systematic errors in ASL" [15]. In fact, since T_1, "the tracer decay rate" is comparable to ATT values (these typically range from 1100 ms - 1400 ms), ATT can prove to be a "major confounding effect" [17]. Hence, modifications to generalize this formula to be true for different ASL methods must be introduced. By utilizing an equation for general tracer kinetics, the following equation is derived:

$$
\begin{aligned}
\Delta M(t) &= 2M_{0A}f \int_0^t c(t')r(t-t')m(t-t')dt' \\
&= 2M_{0A}fc(t) * [r(t)m(t)] \\
&= fA_{eff}
\end{aligned}
\tag{1.9}
$$

where * denotes convolution. The equation depends on the variables $c(t)$, the "normalized arterial concentration of magnetization arriving at the voxel at time t", $r(t)$, "the fraction of tagged water molecules that remain at time t after their arrival", and $m(t)$, "the fraction of the original longitudinal magnetization tag carried by the water molecules that remains at a time t after their arrival in the voxel", with the corrections dependent on the ASL method utilized [15]. The equation can also be simplified by combining all of the kinetic terms into the variable A_{eff}, which is "the effective area of the arterial bolus", or labelled volume [15]. It is also important to include the parameters Δt, the transit delay

10

"from the tagging region to the image slice", T "the duration of the tagged bolus", T_{ex}, the time delay required from when the blood arrives to when it perfuses into the tissue, T_{1A}, the longitudinal relaxation of blood, and the $T1$ of the tissue [15]. The transit delay is dependent on brain size, and age and an incorrect assumption will lead to greatly skewed results [17]. It is also known that stroke can further skew the ATT due to collateral flow and thus emphasize that the overall CBF values are not wholly accurate and moreover represent blood perfusion estimations.

These additional processes are described by:

$$c(t) = \begin{cases} 0 & 0 < t < \Delta t \\ \alpha e^{-t/T_{1A}} \ (PASL) & \Delta t < t < \Delta t + T \\ \alpha e^{-\Delta t/T_{1A}} \ (CASL) & \Delta t < t < \Delta t + T \\ 0 & \Delta t + T < t \end{cases} \tag{1.10}$$

$$r(t) = e^{-ft/\lambda} \tag{1.11}$$

$$m(t) = \begin{cases} e^{-t/T_{1A}} & t < T_{ex} \\ e^{-T_{ex}/T_{1A}} e^{-(t-T_{ex})/T_{1A}} & t > T_{ex} \end{cases} \tag{1.12}$$

Note that Equation 1.10 contains the variable α which corrects for the labeling efficiency [15], [18]. This is because the magnetized protons may not be fully inverted and consequently will recover faster to equilibrium. While seemingly a small detail, this will ultimately alter the overall CBF value and lead to an underestimation of overall perfusion.

Ultimately, combining $c(t), r(t)$ and $m(t)$ back into Equation 1.12 we get:

$$a(t) = 2M_{oA}c(t)r(TI - t)m(TI - t) \tag{1.13}$$

where the integral of $a(t)$ is A_{eff} [15]. This is useful to graph and understand as the

area under the curve, A_{eff} affects the overall measurement, which can lead to significant errors [15]. There is no such form of ASL that is perfect and free from error, as all have their own systemic issues. However, some are better for certain situations and all have their own advantages and disadvantages.

1.2.5   CASL

Continuous Arterial Spin Labeling (CASL) is the earliest form of ASL introduced in 1992 by Detre et al. [16]. As can be gleaned from the title, CASL involves the usage of a continuous inversion of the blood right at the neck with a constant RF pulse. The specific mechanism at play is referred to as *flow driven adiabatic inversion* which was "originally introduced as a blood labeling technique for MR angiography" in which the frequency will cycle through resonances to take advantage of the properties both in phase and out of phase [15], [19]. Essentially, in adiabatic inversion the "effective RF field in the rotating frame is slowly swept from off-resonance to on-resonance and back to off-resonance again" allowing for cleaner inversions [15]. In the case of CASL the motion of the blood itself (flow) produces the sweeping effect instead of varying the RF pulse in a small slice selected area [15]. As the blood flows through this area and the magnetism of the slice select gradient matches that of the RF pulse, the blood is inverted, with the pulse lasting a few seconds in length [18]. This process produces the tagged image. The control image must be approached very carefully because the blood signal is only 1% of the total signal, an error as small as 1% will lead to a 100% error in measurement [15]. The two methods of preventing off-resonance effects in the control image is to use an RF pulse with a frequency different from that of the labeling pulse, or with the sign of the gradient switched [15].

CASL is now the most outdated form for two major reasons. The first drawback is that CASL requires extra hardware (in the form of two different RF coils), as well as "continuous application of RF power, which most current RF amplifiers cannot provide without modification" and additional costs [18]. The second reason this approach has fallen out of

favor, is because of the high energy deposition in tissue and the consequent heating it can trigger [20]. Hence it has been replaced by newer methods.

1.2.6 PASL

In Pulsed Arterial Spin Labeling (PASL), (the method utilized in the Washington University in St. Louis (WUSTL) dataset), a single 180° inversion pulse is utilized instead of a continuous RF pulse [15]. This single labeling pulse spatially selects a certain bandwidth referred to as the *bolus*, or a thick band of labelled blood [15]. However, a PASL specific issue is that the bolus is not a perfect rectangular profile but rather has wings extending out that can leave behind effects on the image plane due to imperfections in the labeling RF pulse profile. To minimize tagging imperfections, there are various modalities, with the main ones utilized being EPISTAR, FAIR, and PICORE. All have their own various strengths and drawbacks. The main drawback of PASL is "that it creates a bolus...with an unknown and relatively short temporal width," which makes converting the perfusion signal to absolute units difficult. Fortunately, this width can become a known variable and even controlled by using a modification of PICORE called QUIPS II [18]. This is done by removing the tail end of the bolus with a slab selective saturation pulse [18]. The details of the PICORE QUIPS II pulse sequence are discussed in the next chapter Figure 2.3.

1.2.7 pCASL

Pseudo Continuous Arterial Spin Labeling (pCASL), is "the currently preferred implementation of CASL [where] the continuous RF is replaced by a long train of slice-selective RF pulses applied at the labeling plane, along with a train of gradient pulses that have a small but non-zero mean value" [18]. This variation is essentially a hybrid version of both CASL and PASL. This has both the usability factor of PASL as no additional hardware modifications are necessary, with the higher SNR and reproducibility, from CASL [18]. This is also the method utilized for the PLA data in this analysis. A comparison of all techniques
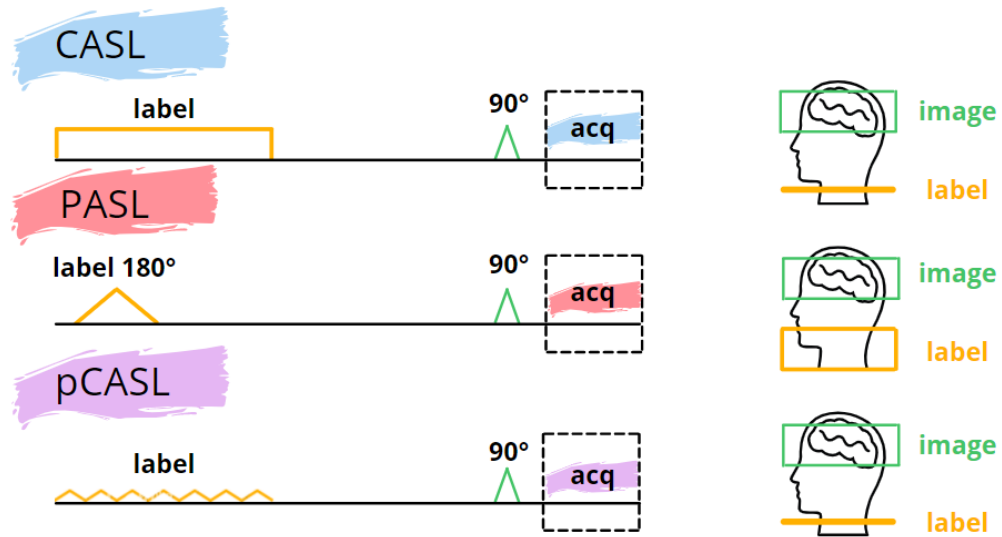
Figure 1.5: Simplified pulse sequence diagrams in order to compare the various ASL methods. CASL = Continuous ASL, PASL = Pulsed ASL, pCASL = Psuedo-Continuous ASL.

mentioned is shown in Figure 1.5.

1.3 Brain Behavioral Maps

Pioneered by Dr. Nina Dronkers and colleagues, Voxel-Based Lesion-Symptom Mapping (VLSM) was created to better understand the relationship between lesion location and behavioral symptoms [21]. The maps created that correlate specific brain areas with behavioral symptoms are referred to as brain behavioral maps. Dronkers et al. created this approach to compare behaviors to the brain in a voxel by voxel analysis [21]. This was a huge step forward in being able to analyze many patients without the constraint that the lesion had to be in the same location, or that the behaviors had to all be the same [21]. Instead, VLSM utilizes continuous behavioral data on a "voxel-by-voxel basis" of structural neuroimaging data [21]. While it is a huge improvement from the prior method of symptom analysis, there are two shortcomings. The first is that VLSM uses a mass-univariate approach to the voxel-by-voxel analysis, meaning that each voxel is treated independently which leads to inaccurate results [22]. This inaccuracy stems from the method's assump-

14

tion that each voxel stands on it's own; the brain actually has many functional networks all intertwined and communicating, meaning that "neighboring voxels often have identical patterns, and produce the same exact statistic" [22]. This was addressed by Pustina et al. in 2017 with their introduction of the multivariate approach, in which voxels are no longer treated independently but as correlated, and instead emphasis is placed upon unique patches [22]. They emphasize this importance stems from the fact that just like the death of a single neuron is unlikely to cause hemiparesis, lesion within a single voxel is unlikely to cause aphasia [22]. Their solution, a multivariate approach referred to as Sparse Canonical Correlation Analysis for Neuroimaging (SCCAN), is based upon canonical correlation analysis methods. Canonical correlations "take two sets of variables" which in this case would be "behavioral scores and voxel values... and search for optimal weights to apply on each side such that one or more common components are created which maximize the relationship between domains" [22]. This was optimized for usage with neuroimaging data in order to create LESYMAP, a program written in R created specifically for the formation of brain behavioral maps for brains with lesions.

Another shortcoming of the mass-univariate approach addressed by Pustina et al. is the discrepancy in lesion to healthy tissue ratio within a single voxel. They describe that "different voxels have different lesion ratios, and, consequently, different statistical power" [22]. This is also taken into account with SCCAN, leading to more accurate results.

While SCCAN offers a vast improvement in terms of the accuracy of lesion-to-symptom mapping, there are still limitations. SCCAN only takes into account the location of the lesion and not the degree of damage, nor does it account for tissue perfusion. In this study, we hope to create the foundation for Voxel-Based Lesion and Physiology to Symptom Mapping (VLPSM) which includes additional information from physiological imaging such as CBF. It is our hope that the inclusion of CBF will create a more holistic view of the brain and add additional insight to make sense of behavioral patterns post stroke. While any behavioral scoring modality may be utilized, the two used in this study are the Hopkins

15

Verbal Learning Test (HVLT) and Brief Visuospatial Memory Test (BVMT) immediate recall, delayed recall and the corresponding T-scores that correct for age differences.

CHAPTER 2

METHODOLOGY

Two datasets were analyzed for this project. The first was a collection of 5 participants with left hemisphere strokes from the PLA study directed by Dr. Lisa Krishnamurthy at the CVNR of the Atlanta Veteran's Affairs Hospital. These stroke patients' ages ranged from 35 to 81, with an average age of 52 years, and 60% identifying as men and the remaining 40% identifying as women.

The second dataset was from the WUSTL based study ran by Dr. Maurizio Corbetta, consisting of stroke patients with various locations and severity. This dataset was narrowed down to 19 participants after selecting only those meeting our requirements of minimal motion artifacts in the T1w and T2w scans, as well as at least 40% of volumes remaining in the pASL scan. We also required easy identification of the lesion, since most lesion masks needed to be drawn by hand and accurately describe the lesion area for reasonable results. The selected participants ranged in age from 22 to 77 with an average age of 55 years, and with 57% identifying as men and 43% identifying as women.

With the datasets combined, we utilized a total of 24 patients' data. However, one of the PLA subjects did not have any behavioral scores, which brought the total number down to 23 participants for the behavioral analysis, and another PLA participant was missing the BVMT delay and corresponding T-score, so only 22 total participants were utilized for that specific analysis.

2.1 Quantifying Structural damage with TIGR maps

2.1.1 Lesion Masks

Lesion masks were either created by a program called LINDA or drawn by hand for the PLA data, depending on how accurate the generated masks were deemed to be. Lesion masks for the WUSTL data were downloaded along with the images. However, it was quickly realized that these masks were drawn onto the acute session scans, whereas we needed them to fit the chronic lesion. This was challenging for a couple reasons: 1) some lesions were much smaller in the chronic MR image and masks needed to be heavily edited and/or completely re-drawn, and 2) some lesions were very difficult to discern from the surrounding tissue (some could not be identified at all, in which case they were excluded from the analysis). An example of a lesion in the acute session (Figure 2.1a) versus the same lesion approximately one year after (Figure 2.1b) is shown below. This is to highlight that the lesion masks from the acute session transplanted onto the chronic session may include too much healthy tissue and requires intensive editing. Because we did not have access to a neuroradiologist that could help identify the lesions in the chronic stage, the resulting masks may not be wholly accurate, and should be considered a possible source of error.

2.1.2 TIGR scoring

The TIGR method relies on the division of T2w image by its corresponding T1w image. Denoising of both T1w and T2w images using an optimized nonlocal means (ONLM) filter by Coupe et. al 2008 to remove Rician noise improves the quantification of the ratio [12], [23].

The T2w image is then coregistered into T1w space. To do this, Freesurfer was run on all T1w and T2w images. Freesurfer is an advanced structural MRI analysis software that helps to partition the brain into white matter, grey matter, and other anatomical structures.

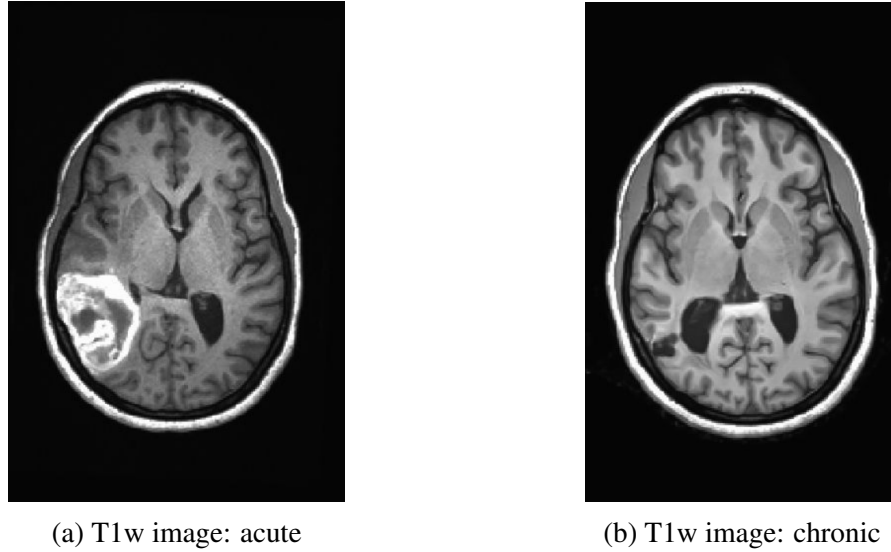(a) T1w image: acute   (b) T1w image: chronic

Figure 2.1: Example of a lesion in the acute scan versus the chronic scan one year later. The snapshot was taken as the same axial location.

This is important for the step of co-registering scans into the same space (i.e. a T2w scan into the space of the T1w scan). The T2w image is then divided on a voxel-by-voxel basis by the T1w image to further highlight the morphology within the lesion [12]. Then, "to compare TIGR maps and functional maps across subjects and generate brain behavior relationships, the T2w/T1w ratio maps are spatially normalized to MNI template space" [12]. In order to create the damage gradient from 0.1 to 1, ten bins total were defined: 0, 0.1, 0.2, 0.3 ... 1, where zero denoted healthy tissue. The threshold for the binning was individualized per participant and determined by their specific GM and CSF values [12]. The low bound of 0.1 is created by the GM threshold empirically at the 50th percentile, with anything lower than this denoted as healthy tissue, and the upper bound of 1 is defined by the CSF threshold empirically at the 5th percentile, with anything above this high bound denoted as "most damaged" [12]. The intermediate damage values were then defined in a "linear fashion" with the upper and lower bounds already set as discussed prior [12]. The overall scoring can then be multiplied by the lesion mask to view just the lesion area, and a visual representation can be shown by utilizing a colorbar to visually inspect the damage gradient as seen in Figure 1.4b. A visual representation of this pipeline can be seen in

Figure 2.2

Unfortunately, this process is not sensitive to hemorrhagic portions of lesion, so these areas were created by inverting the T2w image, segmenting the inverted image, and creating a mask of only the parts with the highest signal. This was then condensed to just the lesion area by multiplying times the lesion mask. In order to be sure there would be no overlap, a binary mask of the TIGR region was subtracted from the hemorrhagic portion, and then they were added together to form the final TIGR mask. Hemorrhagic portions were denoted with a TIGR scoring of 1, after a lit search emphasizing the role hemorrhages cause in the destruction to cellular matrices, and highlighting that such tissue can be considered to be in the same regime as the most damaged tissue and thus numerically labelled as such [24].
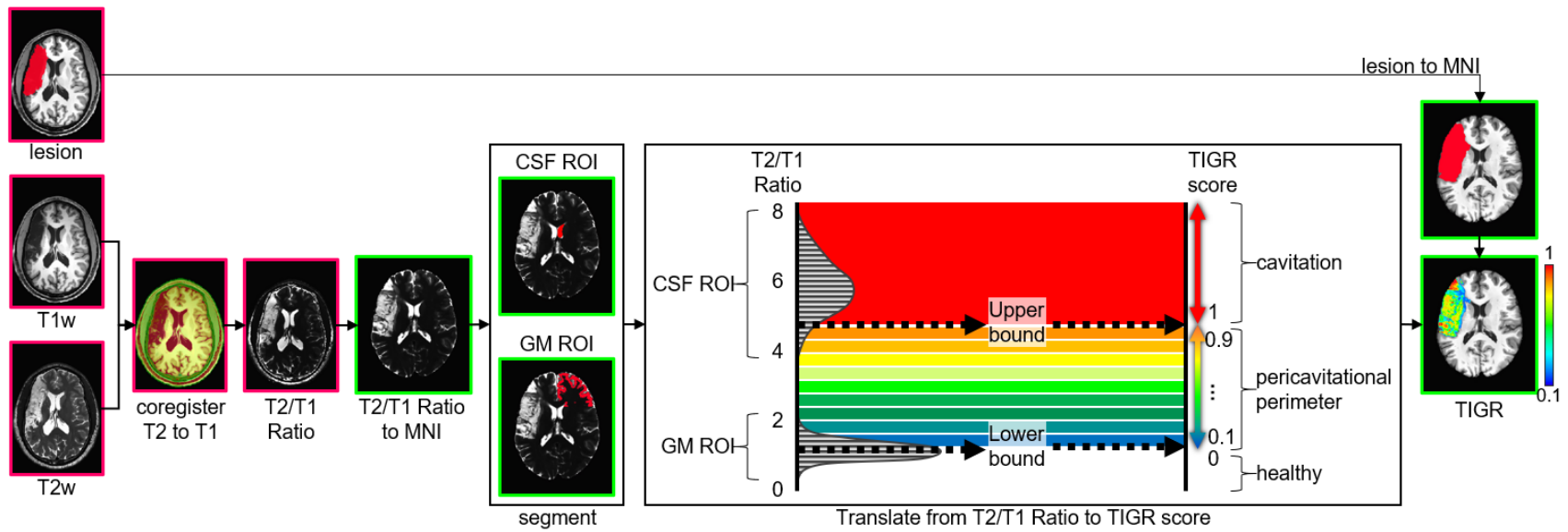
Figure 2.2: Visual representation of the pipeline utilized to create TIGR scores, courtesy of Krishnamurthy et al. [12]
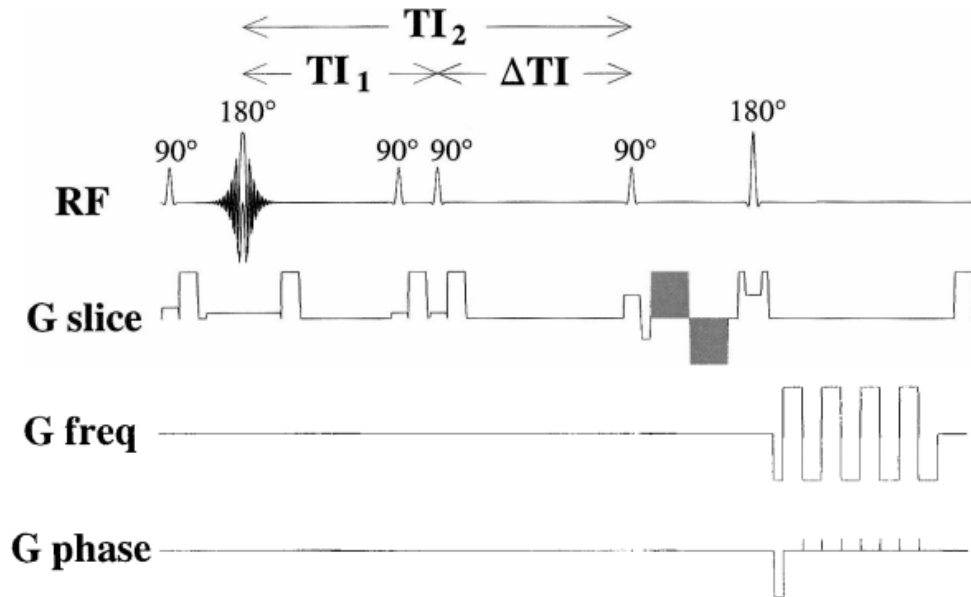
2.2 CBF Maps

Figure 2.3: PASL PICORE QUIPSS II pulse diagram courtesty of Wong et al. 1998 [25].

All of the WUSTL subjects had two PASL scans, hereby referred to as PASL1 and PASL2, whereas the CVNR subjects had one pCASL scan, hereby referred to as pCASL1. The voxel size of ASL1 and ASL2 in native space was 3.438 mm (64 voxels) by 3.438 mm (64 voxels) by 7.500 mm (15 voxels), and that of pCASL1 was 2.973 mm (74 voxels) by 2.973 (74 voxels) by 4.4 mm (35 voxels).

PASL1 and PASL2 were collected by using the PICORE QUIPPS II PASL method, and important parameters include a $TI_1 = 1.6$ s, TI=3.4 s, and a TR = 2.6 s. While the averages of both PASL1 and 2 were utilized to calculate important parameters of the pipeline for more statistical power, analyses afterwards only utilized PASL1 for simplicity.

The pCASL1 scans were collected with the parameters of TR = 5.06 s, labeling duration = 1.5 s, TE = 0.013 s and a PLD = 2.2 s, where PLD stands for the post labeling delay [12]. Because the perfusion signal is small (1 %), adequate SNR is achieved by signal averaging across multiple timepoints. Thus, only those participants with $\geq$ 40% of ASL volumes left

22

after motion censoring were considered for analysis. To optimize how stringent we needed to be for censoring motion, we chose two participants' data, to see how they would respond to a motion censor of 0.5, 0.6, 0.7, 0.8 and 1.

As shown in Figure 2.4a and Figure 2.4b, as motion is censored the SNR improves up until around 0.7 and 0.8 because more volumes means an improved average, but then the SNR begins to decrease as too much motion is allowed to corrupt the signal. The value of 0.7 was chosen as it was the point of inflection for GM and WM in the example participant with minimal movement, and for the WM in the participant with the substantial movement.

The next step was to optimize the rest of the ASL to CBF pipeline. As shown in Figure 2.5 there were 3 pipelines tested. The *First Model*, the *Denoise First* model, and the *No Denoise* model. All steps above the dotted line were performed in native space and all steps below the line were completed in MNI space. All pipelines included bulk-head motion correction which aligned all volumes with 6 degrees of freedom, separated the label and control volumes, censored head motion based on the optimal 0.7 motion threshold, computed the difference signal representing perfusion, conversion of the perfusion signal into absolute physiological units using a single compartment model [18] and a transformation into MNI space. One major difference between the pipelines is that the *First Model* uses a Gaussian smoothing kernel of full width half maximum (FWHM) of 5 mm in native space, whereas *Denoise First* and *No Denoise* bring the smoothing step to the end. Further, because the CBF map is brought into MNI space with a 1x1x1 mm voxel size, we were able to use a smaller smoothing kernel, since typically, a smoothing kernel should be 1.5-2 times the voxel size. Options of 1.5 mm, 2 mm, 3 mm and 4 mm were all tested. Lastly, the *Denoise First* model introduces a denoising step before the bulk head motion correction. The denoising model utilized was the Localized Principal Component Analysis (LPCA) filter, the most efficient denoising filter for a 4D dataset [26]. LPCA works by "a) decomposing the signal into the local principal components, then b) shrinking the less relevant components, and finally c) reconstructing back the signal... the key idea of this
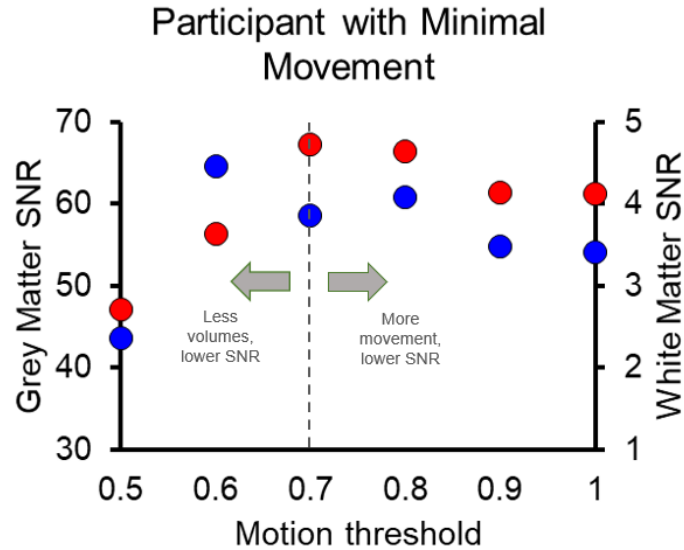
(a) Movement threshold analysis on subject with substantial head movement in ASL. RED = Grey Matter, BLUE = White Matter.
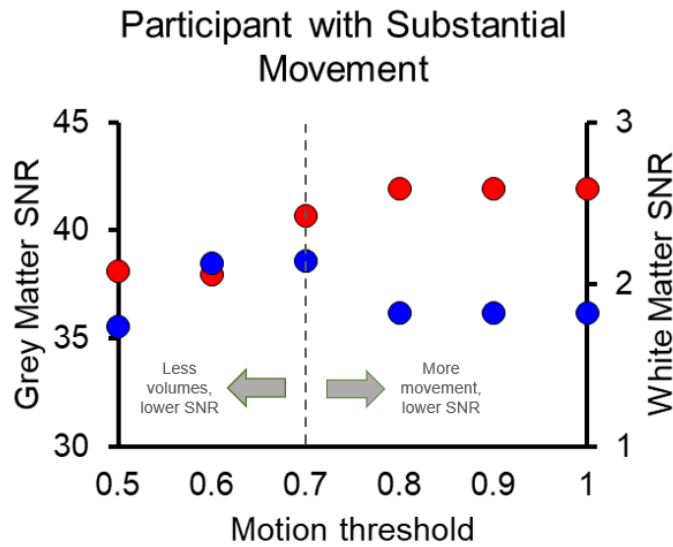
(b) Movement threshold analysis on subjects with minimal head movement in ASL. RED = Grey Matter, BLUE = White Matter.

Figure 2.4: Example of different values for motion thresholding within our pipeline and the effects it had on GM and WM SNR. The red and blue circles represent the GM and WM respectively. Values were taken from the mean of the WM SNR and GM SNR PASL1 and PASL2 scans respectively.

process is the fact that image patterns can be represented as a linear combination of a small number of basis images while the noise, being not sparse will be spread over all available components" and hence can be removed [26].
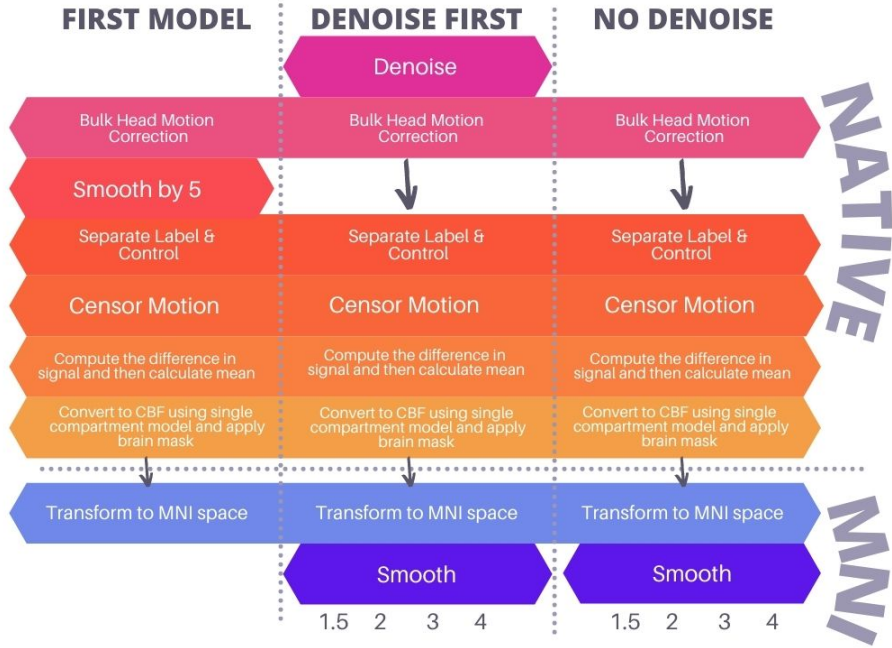
Figure 2.5: Diagram of the 3 ASL to CBF pipelines utilized to optimize results. The steps above the dotted line were enacted in native space, and those below the dotted line were run in MNI space.

The single compartment model utilized for PASL1 and PASL2 is shown in Equation 2.1, and the single compartment model utilized for pCASL1 is shown in Equation 2.2.

$$\text{CBF} = \frac{6000 \cdot \lambda \cdot (\text{SI}_{control} - \text{SI}_{label}) \cdot e^{\frac{\text{TI}}{\text{T}_{1,blood}}}}{2 \cdot \alpha \cdot \text{TI}_1 \cdot \text{SI}_{PD}} \quad [\text{mL/100 g/min}] \tag{2.1}$$

$$\text{CBF} = \frac{6000 \cdot \lambda \cdot (\text{SI}_{control} - \text{SI}_{label}) \cdot e^{\frac{\text{PLD}}{\text{T}_{1,blood}}}}{2 \cdot \alpha \cdot \text{T}_{1,blood} \cdot \text{SI}_{PD}(1 - e^{\frac{-\tau}{T_{1,blood}}})} \quad [\text{mL/100 g/min}] \tag{2.2}$$

The values utilized for the constants in Equation 2.2 and Equation 2.1 are shown in Table 2.1.

2.3 Relating CBF to TIGR

In order to validate the damage gradient, we must provide a physiological parameter (CBF). In order to relate CBF to TIGR, we first separate the TIGR score into binary masks of the

Table 2.1: Table of values utilized in the quantification of pASL data from Alsop 2014 and Krishnamurthy et al [18], [12]

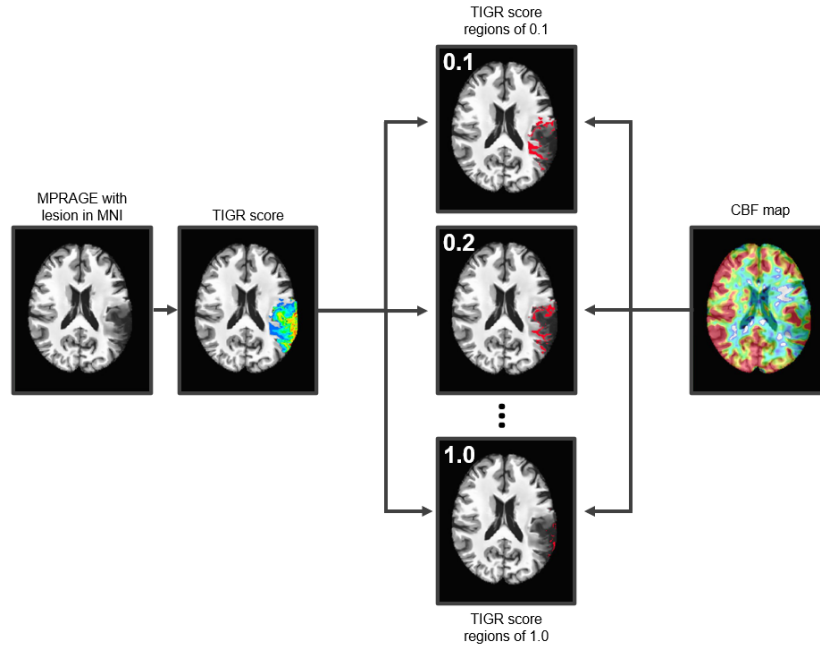| Parameter	Value
λ (blood-brain partition coefficient)	0.9 mL/g
$T_{1,blood}$ at 3.0T	1650 ms
α (labelling efficiency for PASL)	0.98
α (labelling efficiency for pCASL)	0.85
PLD	2200 ms

Figure 2.6: Pipeline to calculate the mean CBF score value per TIGR score bin

respective bins: 0.1, 0.2, 0.3...1. This mask is then overlaid on the CBF mask and the average value of all voxels inside the mask is calculated. A visual example of this pipeline can be seen in Figure 2.6. After completing this for each individual participant, the averages of all participants were combined, and standard error calculated to create the results seen in Figure 3.6. To calculate the mean CBF in healthy tissue for each participant, the TIGR score was binarized and flipped onto the other hemisphere of the brain, and the average value was calculated. This was done instead of taking a whole brain average because each lesion included different ratios of WM and GM which are generally perfused differently. Hence, in order to have the most accurate comparison of the healthy level of perfusion for

the affected part of the brain in that individual, it was important to measure the value for the same region. This allowed an apples-to-apples comparison of CBF values.

2.4 Relating Brain Parameters to Behavior

In order to relate brain parameters to behavior, we utilized a simple univariate analysis method. This was first conducted with TIGR as the only additional input to behavior, and then was repeated with the additional CBF information to see if this additional information could better predict the output. With just TIGR, we modeled our equation as:

$$behavior = a \times \text{TIGR} + c \tag{2.3}$$

and calculated the constants of a and c. With the additional CBF information, this equation became:

$$behavior = a \times \text{TIGR} + b \times \text{CBF} + c \tag{2.4}$$

And we solved for a, b and c. The goodness of fit was then evaluated by calculating the R^2 values.

CHAPTER 3

RESULTS

3.1 Optimizing the CBF Maps

We began by first randomly selecting 11 participants' data to optimize the CBF map pipeline. They were chosen to be a mix of various lesion sizes and locations (right hemisphere lesions vs. left hemisphere lesions) as well as a combination of ischemic and hemorrhagic type lesions. One participant consistently had CBF values ranging from 100-200, values that are not physically possible, so we decided to exclude this participate from the analysis so as not to skew the results based upon this outlier. Another participants had a lesion of an unclear location and was also excluded from the analysis, resulting in a total of 9 subjects' data utilized to optimize the CBF pipeline.

We started by comparing the *First Model* outcome to the *Denoise First* pipeline and the *No Denoise* pipeline. We chose to compare the *No Denoise* and Denoised pipelines to the *First Model* pipeline with a blur of 4 mm as that would be closest to the *First Model*'s smoothing kernel of 5 mm, and would lead to a more fair comparison. Visual representations of the same participant's CBF map can be seen in Figure 3.1a, whereas the pipelines are numerically analyzed in Figure 3.1b.

Of the three pipelines, the *First Model* consistently gave the worst results. Because of the smoothing early on in native space where the images still have quite a large voxel size, nearby voxels greatly changed the values. This can be seen both visually with the poor spatial resolution in Figure 3.1a, but also numerically in Figure 3.1b, as the resultant fit shows a trending increase in blood flow as tissue becomes more damaged, which is counter-intuitive. Thus, the choice was narrowed down to either the *Denoise First* model or the *No Denoise* model.
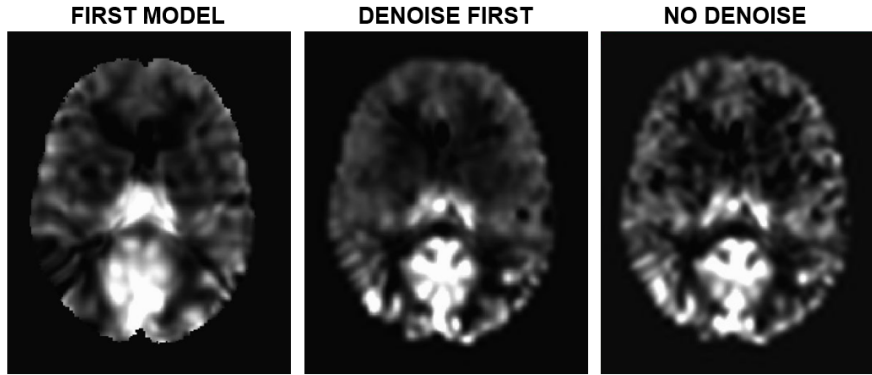
(a) From left to right these CBF images represent the *First Model* with a smoothing kernel of 5, *Denoise First* pipeline with a blur of 4, and the *No Denoise* pipeline with a blur of 4. These were all taken on the same axial slice from the same participant after the CBF map had been transformed into MNI space.
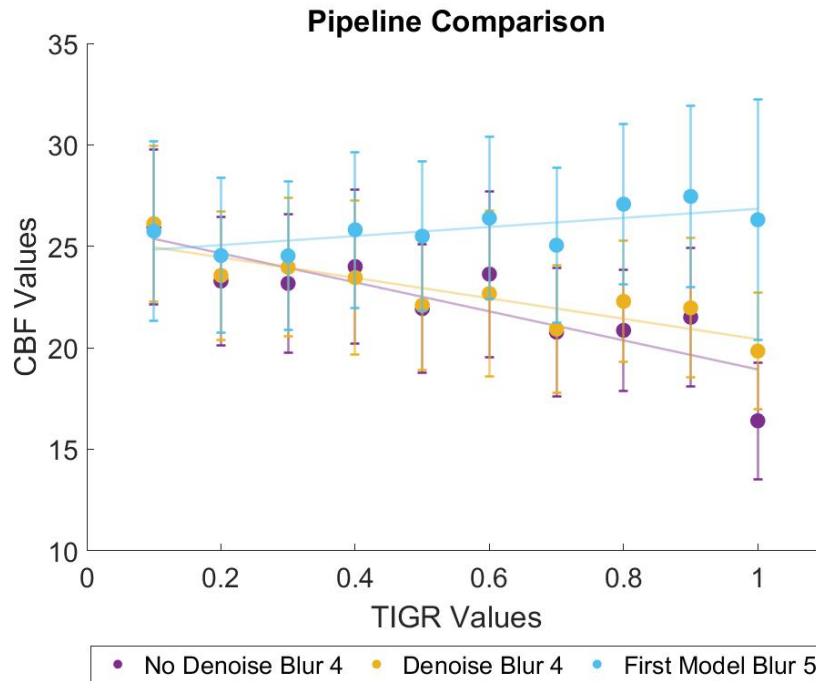
(b) CBF Pipeline Comparison between 9 participants' CBF data from the *No Denoise* pipeline with a blur of 4, Denoised pipeline with a blur of 4, and the *First Model* consisting of a blur of 5. All were fit with a linear regression and had R^2 values of 0.7095, 0.7748, and 0.4674 respectively.

Figure 3.1: Visual and graphed CBF pipeline comparison between the three methods detailed in Figure 2.5

As can be seen in the visual representation, the *No Denoise* pipeline clearly has the best spatial resolution. Further, it also had the steepest decline in CBF values versus TIGR
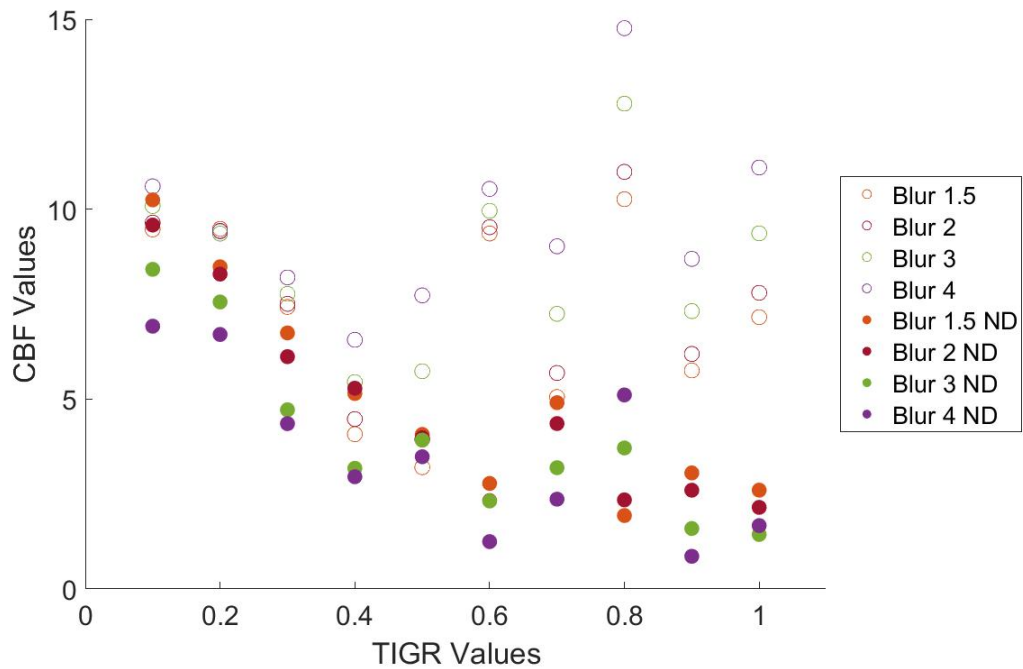
29

Figure 3.2: Representative subject showing *Denoise First* vs. *No Denoise* pipeline results with various smoothing kernels

score, resulting from a stronger signal that the *Denoise First* pipeline diluted. Further support showing why the *No Denoise* pipeline was ultimately chosen is demonstrated in Figure 3.2. Whereas the Denoise pipeline rapidly increased with increasing tissue damage, again a highly unlikely scenario, the *No Denoise* pipeline had much more enlightening results.

After the *No Denoise* pipeline was chosen as the optimal version of computing CBF maps, we then had to choose which smoothing kernel value to use. A comparison graph is shown in Figure 3.4. All smoothing kernels had reasonable linear fits, with significant R^2 values, because all had reasonable spatial resolution as is shown visually in Figure 3.3. Since only one model could be chosen for the analysis and all gave reasonable, statistically significant results, we chose blur kernel FWHM of 2 mm since it resulted in the highest R^2 value and thus the best fit from our model.

BLUR 1.5

BLUR 2

(a) No Denoise Blur 1.5

(b) No Denoise Blur 2

BLUR 3

BLUR 4

(c) No Denoise Blur 3

(d) No Denoise Blur 4
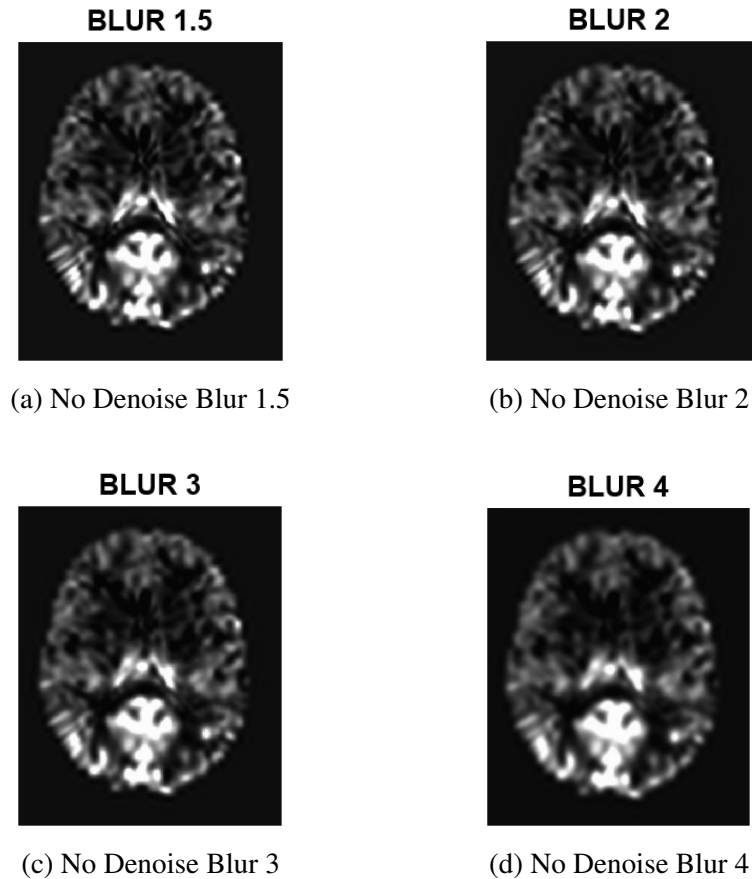
Figure 3.3: Comparison of the smoothing kernels with value 1.5 mm, 2 mm, 3 mm, and 4 mm on the *No Denoise* pipeline CBF images.

3.2 Healthy vs. Lesioned CBF

Once we optimized our pipeline and selected the *No Denoise* pipeline with a blur of 2, we found the average CBF values for all participants' total lesioned tissue and the CBF for the corresponding healthy tissue on the opposite hemisphere of their brain. The resulting boxplots can be seen in Figure 3.5. As expected, the median of the average healthy CBF values was statistically significantly larger than that of the lesioned CBF values, with a p value < 0.005.

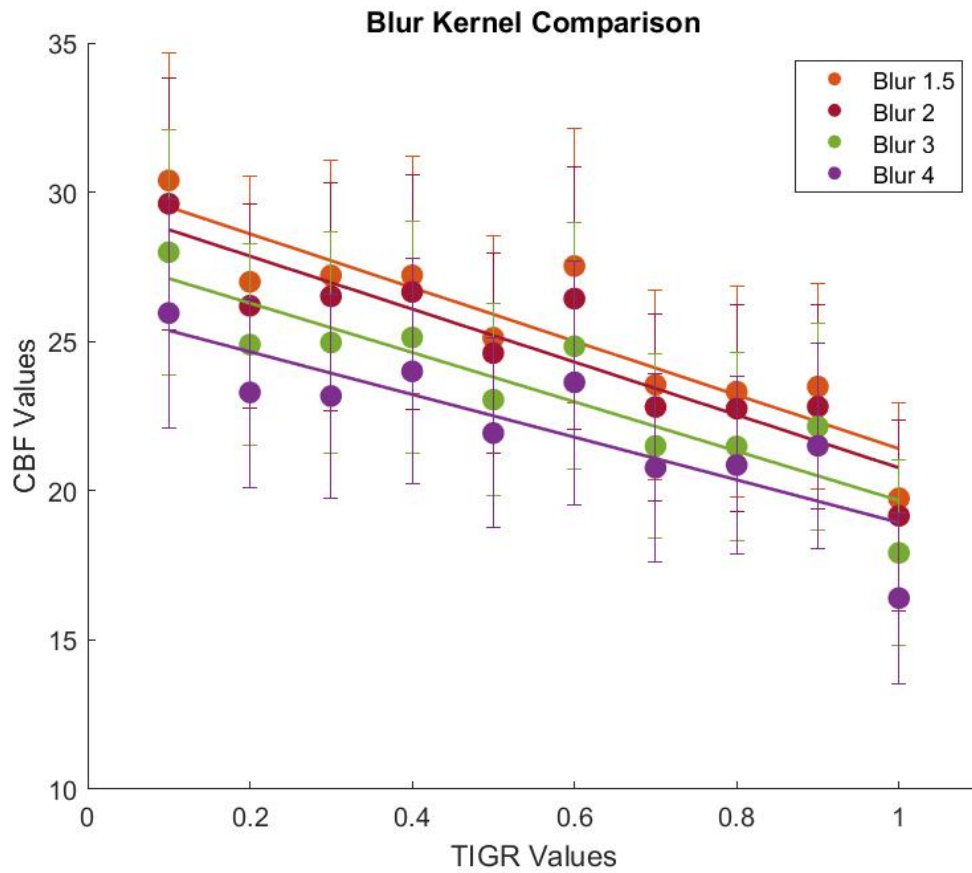Figure 3.4: A comparison between different smoothing kernels on the optimization of the *No Denoise* pipeline. R^2 values for a blur FWHM of 1.5 mm, 2 mm, 3 mm, and 4 mm were the following: 0.8143, 0.8301, 0.8069, and 0.7095.

3.3 TIGR vs. CBF

We also compare the average CBF value within each TIGR scoring bin across 24 participants for the *No Denoise* pipeline with a smoothing kernel of 2 mm. As expected, we observe a significant negative slope between TIGR and CBF showing that on average, with increasing damage, there is a decline in blood flow to the tissue. The error bars shown denote the standard error between participants for each respective bin value. The data was fit with a linear regression shown to be significant, resulting in an R^2 of 0.6256.

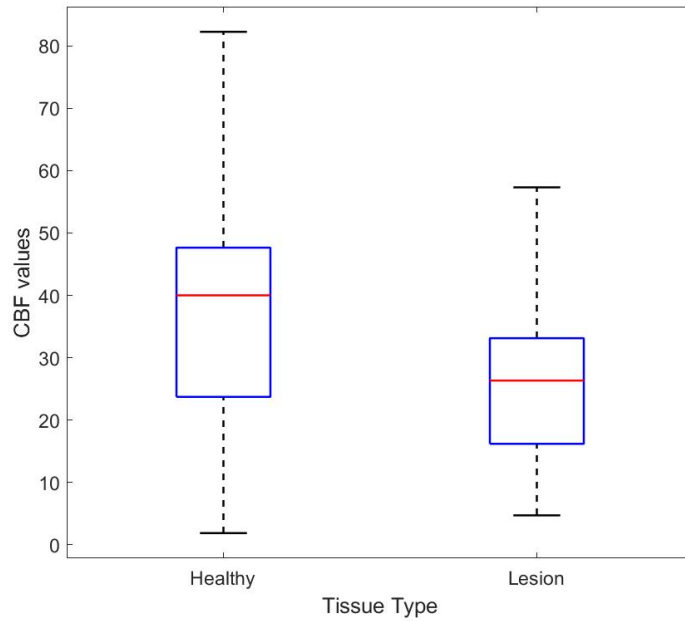Figure 3.5: Boxplot of CBF values in healthy vs lesioned tissue for the *No Denoise* pipeline with a smoothing kernel of 2. The CBF values between the healthy and lesioned tissues are significantly different, with p < 0.005
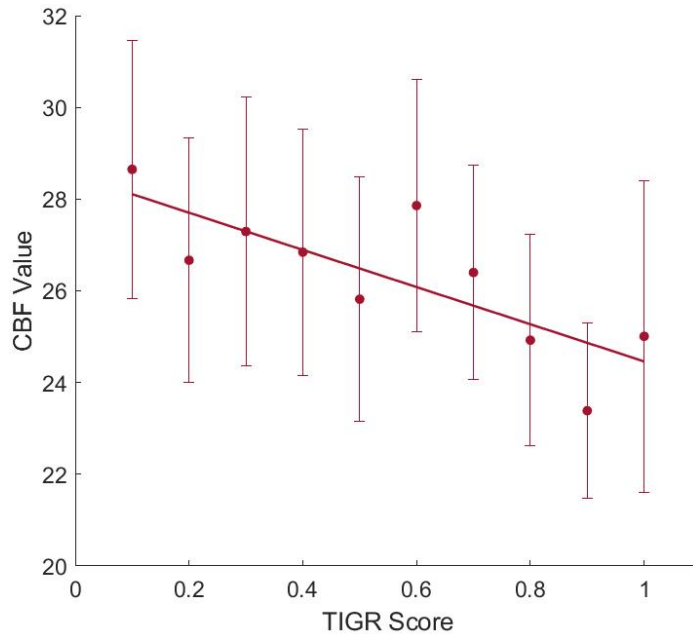

Figure 3.6: Average CBF values for all participants vs. TIGR score within the *No Denoise* pipeline with a smoothing kernel of 2. The linear regression fit to the data points has a R^2 value of 0.6256
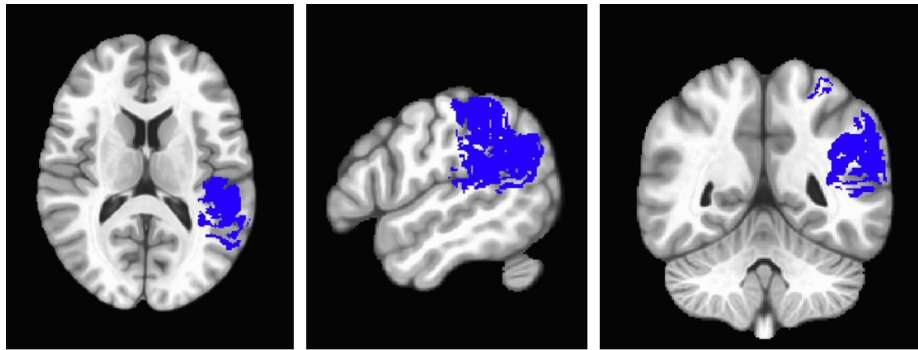
Figure 3.7: ROI example of a region with a negative correlation with the HVLT immediate recall score with TIGR as the only parameter. R^2 was thresholded at 0.2 and has a maximum value of 0.39.

3.4 Creating Brain Behavioral Maps

3.4.1 TIGR Only Univariate Analysis

The next step in our analysis was to relate our TIGR and CBF brain maps to the behavioral scores of each individual patient. Because one of the PLA participants did not have the behavioral scores of interest, this analysis was conducted on 23 participants. First, we utilized only TIGR scoring vs. behavior in order to obtain a baseline of results without physiological parameters involved. While the BVMT results were not significant, nor were HVLT delayed recall scoring, we did see significant results for HVLT immediate recall and the corresponding T-score. The output shown in Figure 3.7 visually shows the output significant ROI that suggest a lesion in this location corresponds to a lower behavioral score; moreover, the greater the damage, the lower the behavioral score. Figure 3.7 was thresholded at an R^2 of 0.2, and has a maximum of 0.39.

3.4.2 Adding in CBF

With the additional information of CBF, the output gives different information. The TIGR output shown in Figure 3.8 has very similar results in size and location to Figure 3.7, with slight variances in shape. The CBF results shown in Figure 3.9 shows 5 separate ROIs (when the R^2 threshold is set to 0.2 and clustered at 1,000 voxels). With the addition of
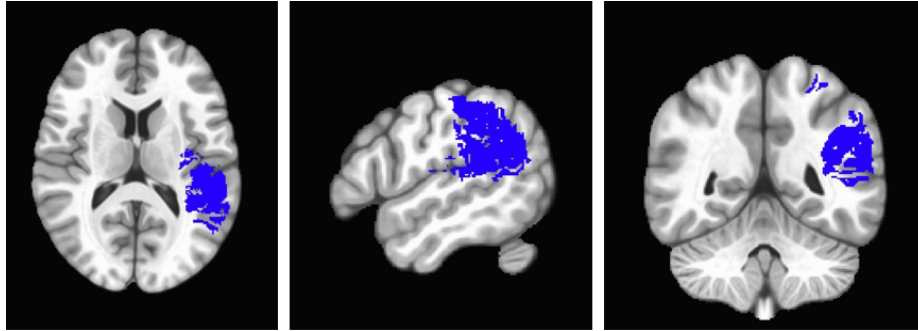
Figure 3.8: ROI examples for the HVLT immediate recall score with TIGR and CBF as parameters, with the TIGR relationship shown. The R^2 threshold is set to 0.2 and the highest significant is 0.63.
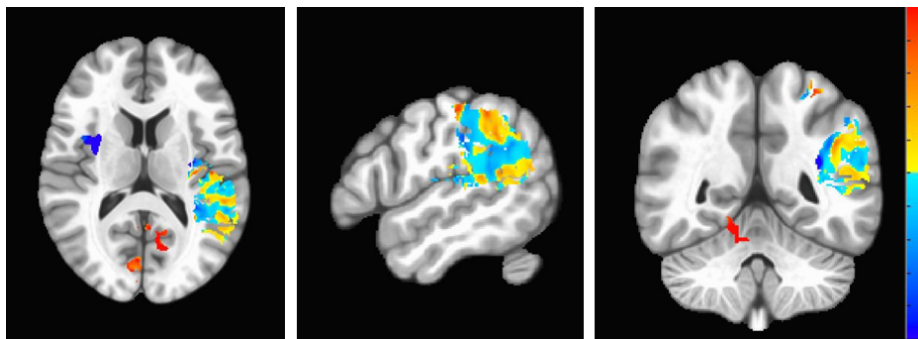
Figure 3.9: ROI examples for the HVLT immediate recall score with TIGR and CBF as parameters, with the CBF relationship shown. The R^2 threshold is set to 0.2 and the highest significant is 0.63.

the CBF, the R^2 increases to 0.63, indicating that the model describes more variance in behavior. Further, CBF identifies areas of positive correlation in addition to the negative correlations seen with TIGR alone. These mark the areas that will increase in behavioral scoring when there is increased perfusion, and will decrease in behavioral scoring when there is decreased blood flow. These results are significantly more powerful than just using TIGR as an input alone, and may be more clinically relevant, as perfusion is something we can directly influence with rehabilitation methods, whereas damage is not.

CHAPTER 4

DISCUSSION

The results of the pipeline optimization show a clear consensus that the *No Denoise* pipeline gives the best signal, as seen by the larger CBF range shown in Figure 3.1b, as well as the better spatial resolution as shown in Figure 3.1b. The improvement from the *First Model* pipeline is clearly due to moving the spatial smoothing kernel from native space and into MNI, since in MNI space the CBF map is warped to a $1 \times 1 \times 1$ voxel size and can be blurred by a smaller amount. In native space, the large voxel size forced us to smooth by a larger value, and then the warped data was brought into MNI space to be further interpolated. There is also a distinction between *Denoise First* and *No Denoise*, again with the latter giving consistently better results. This is most likely due to the fact that the ASL signal is already only 1% of the total signal, so any form of denoising could remove important signal as well [15].

The distinction in CBF between the healthy and lesion tissue is significant, however we believe that if more robust ASL techniques were used, this could be improved greatly. pCASL (as utilized by the PLA data) has been shown to have greater SNR than PASL (as utilized in the WUSTL data), so imaging done with the pCASL technique is encouraged for future work. The Corbetta WUSTL data was also collected over 10 years, beginning around 2010, so the sensitivity of MR Imaging may have been lower. These all could have been factors affecting the quality of the ASL data, ultimately affecting our final results. Other factors that may have been potential sources of error include the single compartment model utilized, as it does not account for separate T1 decay values for the surrounding tissue and blood, but only for blood alone, and the potential increase in ATT for lesioned tissue [18]. Along with being a primary source of error in ASL, ATT greatly increases in an elderly population, which many stroke patients are, and should be taken into account when imaging

this population [27]. We believe these sources may have contributed to the very large values of CBF. It is also important to note other discrepancies between patients may affect our findings. While subjects were randomly selected to be a mix of strokes of different types and sizes, they may not be representative of the whole population due to individual characteristics such as gender, age, prior health complications and any medications. Hence, it is important for this work to be expanded so the results may have higher statistical power and be representative of a larger, more diverse population.

For the TIGR scoring itself, our future work will bring in a radiologist trained in viewing stroke brains who can help create more accurate lesion masks, leading to more accurate TIGR scoring. We would also like to extend the sensitivity of TIGR onto patients with a purely hemorrhagic stroke. Currently, our analysis will only work on a patient with a hemorrhagic stroke if there also exists an ischemic portion. Our future work will also study these lesions at an earlier acute stage, to then tie into our conclusions from the chronic stage, for a better idea of how damage, blood flow and behavioral scoring will progress through time. This will assist in our predictive power, and ultimately be more useful for clinicians seeing patients who have just had a stroke.

In our future work we also intend to improve our brain behavioral mapping methods. First, future modeling may want to test an additional factor if using the mass univariate approach that could account for the CBF-TIGR relationship. An even better approach would be to utilize the more robust multivariate analysis. Our current analysis provides the groundwork for such, and we believe utilizing SCCAN will lead to more accurate results as the assumptions are more based on how the brain actually functions.

Ultimately, we believe our work will increase predictive power in the clinic, and make it easier for physicians to individualize treatment specific to each patient's specific stroke location, size and severity. Since strokes present differently in each individual, any and all interventions must also be individualized. There are many types of rehabilitation methods, and different methods are better for strokes with certain behavioral deficits [28]. Therefore,

by utilizing this information and being able to predict behavioral deficits earlier on and more accurately, clinicians can better plan treatments and start rehabilitation work earlier.

CHAPTER 5

CONCLUSION

In conclusion we have shown that with increasing tissue damage, there is a decrease in CBF both validating the efficacy of TIGR scoring and emphasizing the correlation between tissue damage and blood flow. We have also highlighted that the addition of physiological parameters in creating brain-behavioral maps leads to additional ROIs showing more regions of the brain affected, and increases the statistical power and accuracy of our predictive power. Ultimately, this information will be invaluable for physicians specializing in treating stroke.

Appendices

APPENDIX A

EXPERIMENTAL EQUIPMENT

A 3T MRI at Emory University was utilized to collect T1w, T2w and pCASL scans for the PLA data. All other participants' images were collected at the WUSTL facility in the Corbetta Laboratory.

APPENDIX B

DATA PROCESSING

Linux-based systems within the Atlanta VA CVNR served as our main means of analysis.

All data was processed on said server and kept confidential.

REFERENCES

[1] H. Ghuman, C. Mauney, J. Donnelly, A. R. Massensini, S. F. Badylak, and M. Modo, "Biodegradation of ecm hydrogel promotes endogenous brain tissue restoration in a rat model of stroke," *Acta Biomaterialia*, vol. 80, pp. 66–84, 2018.

[2] P. M. Pedersen, K. Vinter, and T. S. Olsen, "Aphasia after stroke: Type, severity and prognosis," *Cerebrovascular Diseases*, vol. 17, no. 1, pp. 35–43, 2003.

[3] F. G. Birenbaum D Bancroft LW, "Imaging in acute stroke," *The Western Journal of Emergency Medicine*, vol. 12, no. 1, pp. 67–76, 2011.

[4] A. Charidimou, D. Kasselimis, M. Varkanitsa, C. Selai, C. Potagas, and I. Evdokimidis, "Why is it difficult to predict language impairment and outcome in patients with aphasia after stroke?" *Journal of Clinical Neurology*, vol. 10, no. 2, p. 75, 2014.

[5] S. A. Huettel, G. McCarthy, and C. Sonetti, *Functional magnetic resonance imaging*. Sinauer, 2014.

[6] H. Mitchell, T. Hamilton, F. Steggerda, and H. Bean, "The chemical composition of the adult human body and its bearing on the biochemistry of growth," *Journal of Biological Chemistry*, vol. 158, no. 3, pp. 625–637, 1945.

[7] R. W. Brown, Y.-C. N. Cheng, E. M. Haacke, M. R. Thomspson, and R. Venkatesan, *Magnetic resonance imaging: physical principles and sequence design*. Wiley-Blackwell, 2014.

[8] M. E. Ladd, P. Bachert, M. Meyerspeer, E. Moser, A. M. Nagel, D. G. Norris, S. Schmitter, O. Speck, S. Straub, and M. Zaiss, "Pros and cons of ultra-high-field mri/mrs for human application," *Progress in Nuclear Magnetic Resonance Spectroscopy*, vol. 109, pp. 1–50, 2018.

[9] S. Abdulla, *T1, t2 and pd weighted imaging*, https://www.radiologycafe.com/radiology-trainees/frcr-physics-notes/t1-t2-and-pd-weighted-imaging, Accessed: 2021-05-11.

[10] *T1 relaxation*, http://mriquestions.com/what-is-t1.html, Accessed: 2021-05-11.

[11] H. Lu, L. M. Nagae-Poetscher, X. Golay, D. Lin, M. Pomper, and P. C. V. Zijl, "Routine clinical brain mri sequences for use at 3.0 tesla," *Journal of Magnetic Resonance Imaging*, vol. 22, no. 1, pp. 13–22, 2005.

[12] L. C. Krishnamurthy, V. Krishnamurthy, A. D. Rodriguez, K. M. McGregor, G. S. Champion, N. Rocha, S. M. Harnish, S. R. Belagaje, S. Kundu, B. A. Crosson, and

et al., "Not all lesioned tissue is equal: Identifying pericavitational areas in chronic stroke with tissue integrity gradation via t2w t1w ratio (tigr)," *Under Review*,

[13] C. E. Brown, P. Li, J. D. Boyd, K. R. Delaney, and T. H. Murphy, "Extensive turnover of dendritic spines and vascular remodeling in cortical tissues recovering from stroke," *Journal of Neuroscience*, vol. 27, no. 15, pp. 4101–4109, 2007.

[14] M. A. Bernstein, K. F. King, and X. J. Zhou, *Handbook of MRI pulse sequences*. Academic Press, 2004.

[15] R. B. Buxton, *Introduction to functional magnetic resonance imaging: principles and techniques*. Cambridge University Press, 2009.

[16] D. S. Williams, J. A. Detre, J. S. Leigh, and A. P. Koretsky, "Magnetic resonance imaging of perfusion using spin inversion of arterial water.," *Proceedings of the National Academy of Sciences*, vol. 89, no. 1, pp. 212–216, 1992.

[17] J. Wang, D. C. Alsop, H. K. Song, J. A. Maldjian, K. Tang, A. E. Salvucci, and J. A. Detre, "Arterial transit time imaging with flow encoding arterial spin tagging (feast)," *Magnetic Resonance in Medicine*, vol. 50, no. 3, pp. 599–607, 2003.

[18] D. C. Alsop, J. A. Detre, X. Golay, M. Günther, J. Hendrikse, L. Hernandez-Garcia, H. Lu, B. J. Macintosh, L. M. Parkes, M. Smits, and et al., "Recommended implementation of arterial spin-labeled perfusion mri for clinical applications: A consensus of the ismrm perfusion study group and the european consortium for asl in dementia," *Magnetic Resonance in Medicine*, vol. 73, no. 1, 2014.

[19] W. T. Dixon, "Simple proton spectroscopic imaging.," *Radiology*, vol. 153, no. 1, pp. 189–194, 1984.

[20] A. Borogovac and I. Asllani, "Arterial spin labeling (asl) fmri: Advantages, theoretical constrains and experimental challenges in neurosciences," *International Journal of Biomedical Imaging*, vol. 2012, pp. 1–13, 2012.

[21] E. Bates, S. M. Wilson, A. P. Saygin, F. Dick, M. I. Sereno, R. T. Knight, and N. F. Dronkers, "Voxel-based lesion–symptom mapping," *Nature Neuroscience*, vol. 6, no. 5, pp. 448–450, 2003.

[22] D. Pustina, B. Avants, O. Faseyitan, J. Medaglia, and H. B. Coslett, "Improved accuracy of lesion to symptom mapping with multivariate sparse canonical correlations," 2017.

[23] P. Coupe, P. Yger, S. Prima, P. Hellier, C. Kervrann, and C. Barillot, "An optimized blockwise nonlocal means denoising filter for 3-d magnetic resonance images," *IEEE Transactions on Medical Imaging*, vol. 27, no. 4, pp. 425–441, 2008.

[24] J. A. Gaasch, P. R. Lockman, W. J. Geldenhuys, D. D. Allen, and C. J. V. D. Schyf, "Brain iron toxicity: Differential responses of astrocytes, neurons, and endothelial cells," *Neurochemical Research*, vol. 32, no. 10, pp. 1685–1685, 2007.

[25] E. C. Wong, R. B. Buxton, and L. R. Frank, "Quantitative imaging of perfusion using a single subtraction (quipss and quipss ii)," *Magnetic Resonance in Medicine*, vol. 39, no. 5, pp. 702–708, 1998.

[26] J. V. Manjón, P. Coupé, L. Concha, A. Buades, D. L. Collins, and M. Robles, "Diffusion weighted image denoising using overcomplete local pca," *PLoS ONE*, vol. 8, no. 9, 2013.

[27] W. Dai, T. Fong, R. N. Jones, E. Marcantonio, E. Schmitt, S. K. Inouye, and D. C. Alsop, "Effects of arterial transit delay on cerebral blood flow quantification using arterial spin labeling in an elderly cohort," *Journal of Magnetic Resonance Imaging*, vol. 45, no. 2, pp. 472–481, 2016.

[28] J. Gassaway, S. D. Horn, G. Dejong, R. J. Smout, C. Clark, and R. James, "Applying the clinical practice improvement approach to stroke rehabilitation: Methods used and baseline results," *Archives of Physical Medicine and Rehabilitation*, vol. 86, no. 12, pp. 16–33, 2005.

VITA

Clara Glassman was born on August 22nd, 1996, in Los Angeles, CA. She currently lives in Atlanta, GA, where she attends graduate school at Georgia Institute of Technology. She is currently pursuing her Masters in Medical Physics and hopes to make it her life mission to better the world around her.

When she isn't attending lectures or working in the CVNR at the Atlanta VA, she can be found dismantling the patriarchy, reading about mental health and anti-racism, or roller-skating down the beltline.